POLITECNICO DI TORINO
Repository ISTITUZIONALE

Leveraging genetic programming to analyze heat transfer and pressure drop characteristics in open-cell metal foams

Original
Leveraging genetic programming to analyze heat transfer and pressure drop characteristics in open-cell metal foams / Catalano, F., Ferrero, A., Fasano, M., Bergamasco, L.. - In: INTERNATIONAL COMMUNICATIONS IN HEAT AND MASS TRANSFER. - ISSN 0735-1933. - 180:(2026). [10.1016/j.icheatmasstransfer.2026.112629]

Availability:
This version is available at: 11583/3016230 since: 2026-10-02T10:21:52Z

Publisher:
Elsevier Ltd

Published
DOI:10.1016/j.icheatmasstransfer.2026.112629

Terms of use:

This article is made available under terms and conditions as specified in the corresponding bibliographic description in the repository

Publisher copyright

(Article begins on next page)

19 November 2026

International Communications in Heat and Mass Transfer 180 (2026) 112629



Contents lists available at ScienceDirect

International Communications in Heat and Mass Transfer

journal homepage: www.elsevier.com/locate/ichmt



Leveraging genetic programming to analyze heat transfer and pressure drop characteristics in open-cell metal foams

Fabio Catalano [a], Andrea Ferrero [b], Matteo Fasano [a], Luca Bergamasco [a,*]

[a] Department of Energy, Politecnico di Torino, Corso Duca degli Abruzzi 24, 10129 Turin, Italy
[b] Department of Mechanical and Aerospace Engineering, Politecnico di Torino, Corso Duca degli Abruzzi 24, 10129 Turin, Italy

ARTICLE INFO

Dataset link: https://doi.org/10.5281/zenodo.18428937

Keywords:
Metal foams
Heat transfer
Pressure drop
Computational Fluid Dynamics
Machine Learning

ABSTRACT

A numerical analysis of pressure drops and heat transfer characteristics in open-cell metal foams is presented, and predictive correlations relating thermo-fluid-dynamic performance to foam topology and flow conditions are proposed. The new possibilities offered by additive manufacturing in terms of cell geometry customization have in fact expanded the design parameter space for metal foams. Consequently, surrogate models able to account for specific geometrical features are required. For this purpose, a large dataset of cells was generated from a broad variety of configurations, resulting in a total of 540 simulations. The numerical simulations were conducted in laminar flow conditions, using air as the heat transfer fluid. The flow patterns within the cells were analyzed, to uncover the mechanisms driving the observed heat transfer and pressure drop behavior. From this extensive dataset, predictive correlations were derived for key performance indicators, including the friction factor, Nusselt number, and area goodness factor. Correlations were developed through symbolic regression, implemented using genetic programming. Unlike conventional regression approaches based on predefined functional forms, this approach derives thermo-hydraulic correlations directly from the data. The proposed correlations were then assessed against selected experimental and numerical datasets from the literature, including porous structures and cell geometries not represented in the regression dataset. The proposed protocol is intended to provide both a better understanding of how geometric and fluid dynamics parameters influence the performance of 3D printable metal foams, and how Machine Learning techniques can be helpful towards design of improved heat exchangers.

1. Introduction

Thanks to their lightweight porous structure, open-cell metal foams offer interesting characteristics for applications where enhanced heat transfer is important, such as design of improved heat exchangers [1,2] and heat sinks [3,4]. Depending on the target morphology, metal foams can be obtained via different production methods [5]. Among these latter, additive manufacturing is an emerging field due to the exceptional possibilities it provides for generating complicated 3D shapes, and for customizing the material characteristics [6–8].

Several lattice structures have been proposed as representative cell designs for heat transfer applications. These include: Weaire–Phelan structures, Laguerre–Voronoi foams, cubic cells, face diagonal-cube structures and Kelvin cells [9]. Kelvin cells, particularly, have been extensively studied due to their simple structure, which makes them a suitable choice for representing open-cell metal foams in heat exchanger designs [10–13]. The ability to design and fabricate these complex structures using additive manufacturing not only enhances the performance of heat exchangers but also opens new opportunities for innovative thermal management technologies. However, while the thermal performance of heat exchangers based on metal foams may be potentially superior to that of traditional heat exchangers, the pressure losses are also generally increased [2]. Indeed, the performance evaluation of these systems should always consider the trade-off between heat transfer enhancement and pressure losses, making an accurate thermo-hydraulic characterization essential for their practical application in compact heat exchangers. Similar thermo-hydraulic optimization challenges have also been addressed for other classes of heat exchangers through advanced CFD simulations, conjugate heat transfer analyses and geometry optimization techniques, further highlighting the importance of predictive modeling in thermal system design [14–19].

* Corresponding author.
E-mail address: luca.bergamasco@polito.it (L. Bergamasco).

https://doi.org/10.1016/j.icheatmasstransfer.2026.112629

Available online 22 September 2026
0735-1933/© 2026 The Authors. Published by Elsevier Ltd. This is an open access article under the CC BY license (http://creativecommons.org/licenses/by/4.0/).

Nomenclature

Latin symbols

A_{sf}	solid–fluid interface area [m^2]
AV_{ratio}	surface area-to-volume ratio [m^{-1}]
$\widetilde{AV}_{ratio}$	dimensionless surface area-to-volume ratio
Bi	Biot number
c_p	specific heat capacity [J/(kg K)]
d	ligament diameter [m]
d_p	pore diameter [m]
D_h	hydraulic diameter [m]
f	friction factor
gdn	area goodness factor
h	convective heat transfer coefficient [W/(m^2 K)]
Hg	Hagen number
j	Colburn factor
L	characteristic length [m]
L_z	cell length along the flow direction [m]
l_{eff}	effective ligament length [m]
$\widetilde{l}$	dimensionless total ligament length
N_p	number of planes used for averaging
Nu	Nusselt number
p	pressure [Pa]
Δp	pressure drop [Pa]
PPI	pores per inch
Pr	Prandtl number
r	ligament radius [m]
$\widetilde{r}$	dimensionless ligament radius
Re	Reynolds number
T	temperature [K]
u	velocity [m/s]
V	volume of the cell [m^3]
z_f	cell elongation ratio (flow-direction length to transverse width)

Greek symbols

α	thermal diffusivity [m^2/s]
ε	porosity
λ	thermal conductivity of the fluid [W/(m K)]
λ_s	thermal conductivity of the solid [W/(m K)]
μ	dynamic viscosity [Pa s]
ν	kinematic viscosity [m^2/s]
ρ	density [kg/m^3]
φ	specific heat flux [W/m^2]

Subscripts

b	bulk
c	cell length
d	ligament diameter
D_h	hydraulic diameter
sol	solid
tot	total
v	volumetric
w	wall

Numerous studies have investigated the heat transfer and fluid flow characteristics in open-cell foams and porous structures, focusing on variables such as porosity, pores per inch (PPI), conductivity of the material, shape of the ligaments and unit cell morphology. A foundational study by [20] demonstrated improved heat transfer in copper foams due to higher thermal conductivity, and provided empirical correlations for heat transfer and pressure drop. Similarly, correlations based on Reynolds or e.g. Hagen numbers have been proposed by other authors [21–23]. Simulation studies employed idealized geometries as Kelvin cells [24,25] and more realistic micro-CT reconstructions [26–28] to assess thermal and hydraulic performance, often revealing that real structures differ significantly from ideal ones in pressure drop and heat transfer characteristics. High porosity generally reduces pressure drop but may reduce heat transfer, though increased PPI tends to improve heat transfer due to higher surface area [29,30]. Structural aspects like ligament shape and strut convexity or tapering [28,31] were shown to significantly affect both pressure drop and heat exchanger efficiency. The flow regime was another critical factor; for instance, laminar regimes exhibited distinct thermal behaviors depending on boundary-layer or stagnant conduction dominance [32], while turbulent regimes were also explored using numerical simulations in representative configurations [33,34]. Comparative analyses of various unit cell types (e.g., Kelvin, Octet, Cubic) found notable differences in thermal performance and flow resistance, with metrics such as area goodness factor and efficiency index used to rank geometries [35,36]. Advanced designs, including functionally graded foams and geometries with variable porosity or extended throats, achieved substantial performance improvements [10,37]. Moreover, the impact of additive manufacturing (AM) processes on foam performance was noted, especially regarding discrepancies caused by cell clogging or morphological defects [38,39]. Surface roughness can also affect heat transfer and pressure drop [40]. Several studies also validated numerical models with experimental data, underscoring the importance of accurate geometry reconstruction (e.g., [41,42]). More recent studies have further confirmed the key role of pore-scale geometrical parameters in enhancing heat transfer performance in metal foams, highlighting the strong dependence of thermo-hydraulic behavior on microstructural features [43–45].

Clearly, the new possibilities provided by additive manufacturing in terms of geometrical customization of the cells also expand the parameter space in which the desired cell characteristics can be optimized. Indeed, while most of the conventional optimization primarily relies on porosity or PPI, thanks to the enhanced manufacturing capabilities it is now possible to modify the geometric features that also play a role such as cell topology, cell elongation along the flow direction or even the strut geometry to optimize the target thermal-fluid dynamic characteristics. Such expansion of the parameters available for performance tuning has led to the need for efficient optimization algorithms and, ultimately, for surrogate model development in terms of correlations able to take key parameters into account, extending beyond classical empirical formulations commonly reported in the literature [46]. This scenario perfectly fits with modern Machine Learning (ML) techniques, which provide several tools suitable for the problem at hand, including data-driven predictive models based on Artificial Neural Networks [47–49], as well as evolutionary optimization algorithms coupled with CFD simulations for the automated optimization of geometrical and operating parameters [50]. Sequential Learning techniques have also been successfully employed for the multi-variable optimization of complex energy systems [51,52]. In the present study, genetic programming and symbolic regression are used to develop closed-form analytical correlations for the thermo-hydraulic performance of various open-cell metal foams, based on data obtained from numerical simulations.

To the latter end, the pressure drop and heat transfer were numerically investigated within a representative volume of a 3D printed lattice designed for solid–fluid heat exchange across a broad range of geometries. Here, 18 different unit cell topologies were considered, each with 5 different porosities and 6 different elongations along the fluid direction. The extensive dataset generated from these simulations was used to derive new correlations for both pressure drop and heat

transfer within the 3D printed lattice. These correlations aim to help a better understanding of the thermal fluid dynamic behavior of 3D printed cells, and thus ultimately of heat exchangers, contributing to more efficient and optimized designs for various industrial applications.

The remainder of the paper is as follows. Section 2 presents the geometries, the adopted physical model, the computational methods and the regression algorithm. The results, which include the validation of the numerical model, the analysis of the flow and thermal characteristics for different geometries and the proposed correlations are reported in Section 3, along with a discussion of the related confidence level obtained. Finally, the conclusions on this work are drawn in Section 4.

2. Materials and methods

2.1. Cell geometries

The analyzed dataset included 18 different unit cell geometries, each of which was characterized by 5 distinct porosity values and 6 elongation factors, resulting in a total of 540 configurations. The geometries considered in this study are idealized and do not include surface roughness or manufacturing-induced defects, allowing the effects of topology on thermo-fluid performance to be isolated. The main unit cell geometries (see Fig. 1) included the following groups: cubic (including cube, face diagonal cube, body-centered cube, face-centered cube, and full cube), octet (including octet, octahedron, V-octahedron, cross-octahedron, and body-centered octahedron), truncated cubic (with variants such as truncated cube, and truncated cube 3 and 4, where the ligaments correspond to the edges of a cube with truncated vertices), hexagonal (one configuration without ligaments on the inlet and outlet faces, and another with all connections between the vertices of the hexagonal faces), rhombicuboctahedron, diamond, and Kelvin cell. The examined porosity range was ε = 0.8, 0.85, 0.9, 0.95, and 0.98. The elongation factor $z_f = L_z/L_x$, defined as the ratio between the dimension of the cell along the fluid-flow direction (L_z) and that perpendicular to it (L_x), was varied at 1.0, 1.3, 1.5, 2.0, 2.3, and 2.5.

To define a unit cell, three key parameters were required: the cell geometry, the elongation factor, and the radius of the struts. The geometry of the unit cell was specified using Cartesian coordinates for the lattice points, along with a connectivity matrix to define the grid. The coordinates of these points were functions of the elongation of the cell along the flow direction z. Since the struts are independent of the fluid flow direction, the connectivity matrix is triangular. With the positions of the points and their connections established, the radius of the struts r for a given target porosity ε can be obtained from the approximation:

$$V_{sol} = V_{tot}\,(1-\varepsilon) \approx \pi r^2 l_{\mathrm{eff}}, \tag{1}$$

where V_{sol} and V_{tot} are the solid and total volumes of the unit cell, and l_{eff} the effective length of the struts, which accounts for their relative positions within the unit cell. For example, a strut with length l that lies on a cell face contributes half of its volume to the cell, with the remaining half contributing to the adjacent cell. Accordingly, its effective length within the unit cell is considered half its total length. Similarly, a strut located on the edge of the unit cell has an effective length equal to one-quarter of a fully enclosed strut. The unit cells were designed using the CAD software Ansys SpaceClaim [53]. Each strut was modeled as a cylinder with radius r and, at each vertex, a sphere with the same radius as the struts was added to fill the gaps. The resulting exact porosity was then calculated directly in the CAD software as $\varepsilon = (V_{tot} - V_{solid})/V_{tot}$. A dedicated Python script for Ansys SpaceClaim was developed to automatically read the cell parameters from an external file and generate the final geometry of the cells. The complete list of all the cells and the Python scripts developed to generate the geometries and calculate the aforementioned parameters are provided in the Supplementary Data file.

Table 1
Mesh independence study. The relative error was computed with respect to the finest mesh.

Cells	Δp (Pa)	Error (%)	Nu	Error (%)
633 948	1813	11.99	30.653	2.37
831 117	1859	9.76	30.618	2.25
1 080 795	1902	7.67	30.408	1.55
1 449 163	1943	5.68	30.682	2.47
2 024 862	1982	3.79	30.408	1.55
3 153 072	2022	1.84	30.222	0.93
5 258 295	2051	0.44	30.024	0.27
6 632 082	2060	0.00	29.943	0.00

2.2. Computational domain and mesh

After designing the cell geometries, the computational domain was created. In order to avoid possible influence of boundary conditions on the results, an entry and an exit region were added along the flow direction. Particularly, the length of the inlet region, which is the distance between the cell inlet highlighted in red in Fig. 2 and the domain inlet, was set equal to the cell width. The outlet region, defined similarly, was set as twice the size of the cell width. The inlet and outlet boundaries of the unit cell are defined by two planes perpendicular to the nominal flow direction and passing through the foremost and rearmost points of the ligament axes, respectively. The lengths of the inlet and outlet extensions were determined through a domain independence study. The inlet extension was varied from 0.2 to 3 times the cell width, while the outlet extension ranged from 0.6 to 6 times the cell width. The selected dimensions were those ensuring domain-independent numerical predictions. A detailed analysis of the flow conditions was carried out to ensure that the flow was able to adapt to the cell geometry at entry and exit, ensuring that it remained independent of the inlet and outlet conditions. This approach was chosen as it was already adopted in other works that have been used for validation of the numerical models [25]. For the complete domain independence study see Supplementary Section S1.

The mesh for the simulations was then generated using the Meshing Module of the Ansys Workbench. A tetrahedral discretization was adopted, with a base-to-max element size ratio equal to 1:2, and a growth rate of 1.1. The curvature normal angle was set to 18°, meaning that each cylinder section is divided into 20 segments. An overview of the mesh for the whole computational domain and a detailed view of the mesh in the proximity of the cell walls are provided in Fig. 3. A mesh independence study was carried out prior to the parametric analysis to assess the influence of the spatial discretization on the numerical predictions. The refinement was performed by progressively reducing the minimum curvature and defeature sizes in the meshing procedure, while keeping the remaining meshing parameters unchanged. The pressure drop across the cell and the average Nusselt number were adopted as convergence metrics. The study was conducted on both the Cube and Octet unit cells, selected as representative of the simplest and the most geometrically complex topologies considered, respectively. Since the Octet cell required the finest discretization to achieve mesh-independent results, the corresponding mesh settings were adopted for all the investigated geometries. The mesh independence study for the octet unit cell is reported in Table 1, while the complete study for both geometries is reported in the Supplementary Section S2. The pressure drop is defined as the difference between the area-averaged pressure at the inlet and outlet of the cell. The meshes are ordered from the coarsest to the finest discretization. The second-to-last mesh was selected for the subsequent simulations, as the differences with respect to the finest mesh were below 0.5% for both the pressure drop and the Nusselt number.

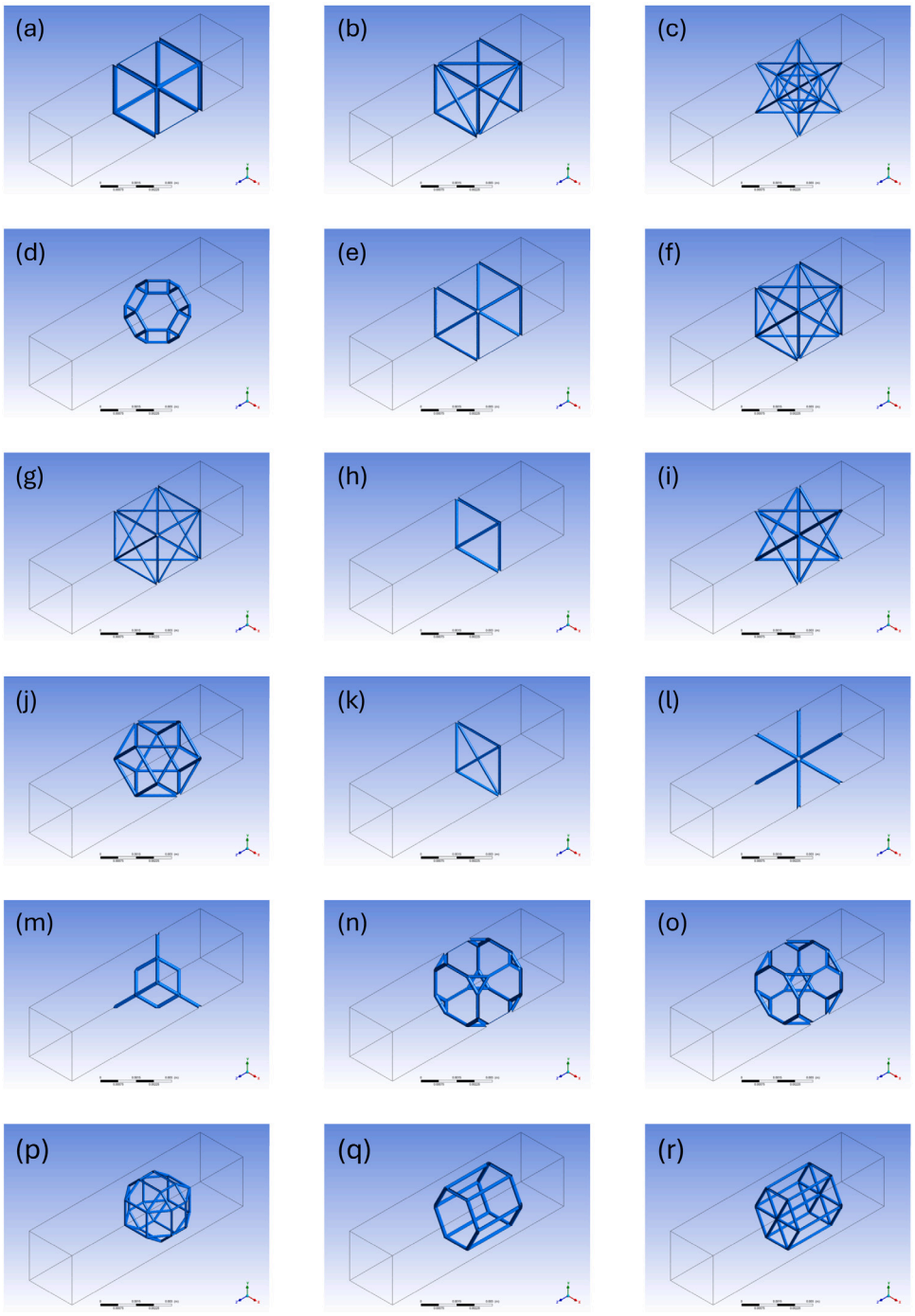


Fig. 1. Overview of the analyzed geometries: (a) Cube cell; (b) FD-Cube cell; (c) Octet cell; (d) Kelvin cell; (e) SC-BCC truss cell; (f) SC-FCC truss; (g) SC-Full truss; (h) Octa cell; (i) V-Octet cell; (j) T-Cube cell; (k) Octa cross cell; (l) Body center cell; (m) Diamond cell; (n) Truncated Cube4; (o) Truncated Cube3 cell; (p) Rhombicuboctahedron cell; (q) Hexagonal-empty cell; (r) Hexagonal cell. The porosity is $\epsilon = 0.981$ for all cells, except for the (o) Truncated Cube3 cell (which is $\epsilon = 0.982$).

2.3. Physical model

The fluid flow in the computational domain is modeled using the steady, incompressible version of the Navier–Stokes-Fourier system of equations, that is

$$\nabla \cdot \mathbf{u} = 0, \tag{2}$$

$$\rho \mathbf{u} \cdot \nabla \mathbf{u} = -\nabla p + \mu \nabla^2 \mathbf{u}, \tag{3}$$

$$\mathbf{u} \cdot \nabla T = \alpha \nabla^2 T \tag{4}$$

with $\mathbf{u}$ being the velocity field, p the pressure, T the temperature, μ and α the dynamic viscosity and thermal diffusivity of the fluid (assumed both constant) respectively.

At the inlet boundary (see Fig. 2), a constant temperature and a constant velocity along the z direction are imposed. At the outlet boundary, an outflow condition with imposed reference pressure is adopted. At the interface between the fluid and the struts of the cell, a no-slip boundary condition is imposed for momentum, and a constant specific heat flux was set. This latter condition is common in pore-scale numerical studies targeting the analysis of heat transfer coefficients [34]. Moreover,

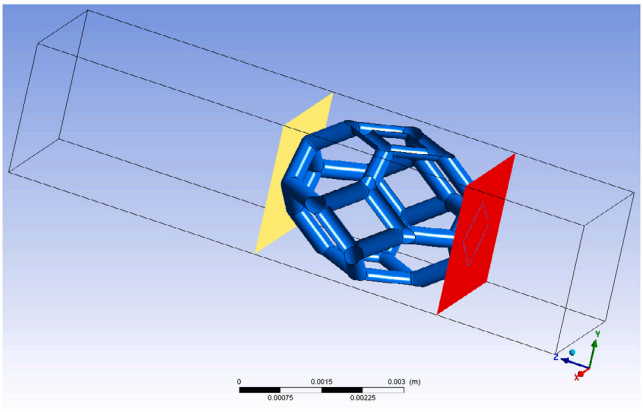


Fig. 2. Unit cell of a representative 3D printed lattice (Kelvin cell with porosity $\varepsilon = 0.9$) for solid–fluid heat exchange. The boundaries of the simulated domain are depicted with black lines, while the solid struts of the 3D printed cell are represented in blue. The cell inlet and outlet planes for the fluid flow are highlighted in red and yellow, respectively (note that, these latter planes do not coincide with the inlet and outlet boundaries of the domain).

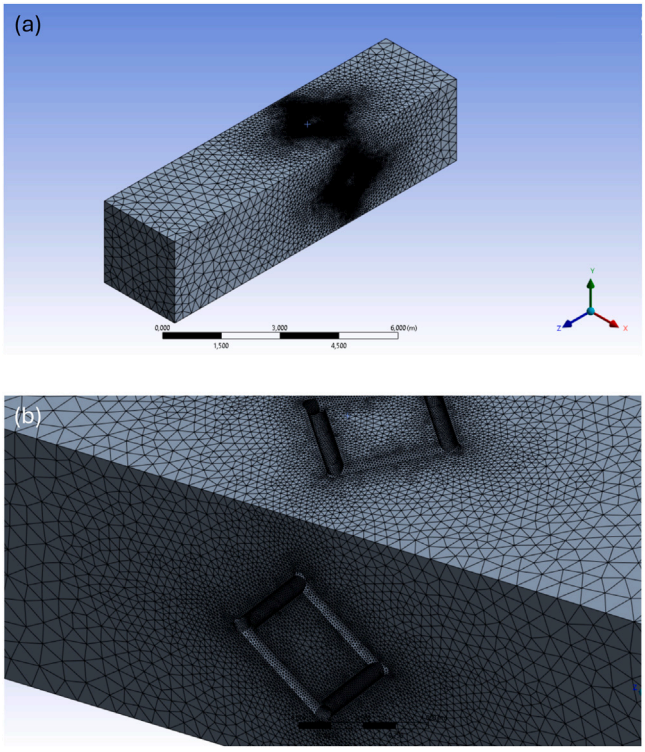


Fig. 3. Meshing of the computational domain: (a) overview of the mesh of the whole domain for a Kelvin cell; (b) detail of the mesh in the proximity of the Kelvin cell geometry.

solving only the fluid domain is justified because, for metallic ligaments in forced convection, internal conduction in the solid is not typically rate limiting. This can be quantified using the Biot number $\mathrm{Bi} = hr/\lambda_s$, where the strut radius can be taken here as the characteristic length. Considering a conservatively-low thermal conductivity of the solid (λ_s) in the order of $\sim$ 15 W/(m K) for e.g. stainless steel (for Al- and Cu-based foams it would be much higher), and that the maximum typical heat transfer coefficients (h) range below 10^3 (here around 5×10^2 W/(m^2 K)), the Biot number typically ranges below 0.1, which supports negligible internal temperature gradients in the solid [54].

On the lateral sides of the domain, boundary conditions were set according to the different unit-cell types that were considered: if the cells had symmetry planes perpendicular to the x and y axes passing through the cell center, a periodic boundary condition along the parallel side planes was set; otherwise, a symmetry boundary condition for the planes perpendicular to the x and y axis was imposed. An overview of the adopted boundary conditions is reported in Table S3.

Simulations were carried out using the Computational Fluid Dynamics (CFD) software Ansys Fluent [55], which relies on the Finite Volume Method (FVM) for the numerical solution. The SIMPLE algorithm was chosen for the pressure–velocity coupling [56]. A second order upwind scheme was adopted for momentum and energy equations, and a second order scheme was used for pressure. The convergence thresholds were set to 10^{-4} residual on the continuity equation, 10^{-6} for each component of the velocity along the three axes, and 10^{-8} for energy. In those cases where convergence criteria could not be achieved, a total of 2000 iterations were carried out. However, these latter simulations were not included in the dataset to derive the correlations (only simulations meeting the convergence criteria were indeed used for regression purposes). The scripts to set up the simulations with common parameters and run the simulations in batch mode are provided in the Supplementary Data file.

2.4. Operating conditions

The simulations were carried out using air as working fluid, with constant thermophysical properties. The inlet flow velocity was imposed as a uniform profile, the inlet temperature was prescribed at 300 K, and a zero-gauge pressure was imposed at the outlet. A uniform heat flux equal to 500 W/m^2 was applied on the solid surfaces. The Reynolds number based on the strut diameter (Re_d) was varied between 5 and 100.

2.5. Post-processing

The cell inlet plane, not to be confused with the domain inlet, was defined as the plane perpendicular to the fluid flow direction passing from the first point of the solid cell encountered by the flow (Fig. 2, red plane). Similarly, the cell outlet plane was defined using the last point encountered along the flow direction (Fig. 2, yellow plane). The bulk temperature of the fluid is the average temperature that would result if the fluid was thoroughly adiabatically mixed [57]. This definition is required for heat transfer problems in ducts and pipes, where the temperature of the flow is not constant even in steady state conditions, but depends on the position. Considering ideal fluid properties, the bulk temperature T_b can be computed as [57]:

$$T_b = \frac{\int_A \rho c_p u T \, dA}{\int_A \rho c_p u \, dA}, \tag{5}$$

where ρ is the density, c_p is the specific heat, u is the local fluid velocity in the streamwise direction, corresponding to the z axis in the present simulations, and A is the considered flow cross-section. For constant ρ and c_p, the bulk temperature reduces to

$$T_b = \frac{\int_A u T \, dA}{\int_A u \, dA}. \tag{6}$$

The (average) convective heat transfer coefficient (h) can then be computed as [25]:

$$h = \frac{\varphi}{\overline{T}_w - \overline{T}_b}, \tag{7}$$

where φ is the specific heat flux exchanged across the solid–fluid interface. The average wall temperature is

$$\overline{T}_w = \frac{1}{A_{sf}} \int_{A_{sf}} T_w \, dA, \tag{8}$$

where A_{sf} is the solid–fluid interface area, and T_w is the solid wall temperature. Note that the specific heat flux φ was the same for all simulations, as it was imposed as boundary condition. Eq. (7) uses the length-averaged bulk temperature

$$\overline{T}_b = \frac{1}{N_p}\sum_{i=1}^{N_p} T_{b,i}, \tag{9}$$

which was calculated in the discrete domain of the simulations as the average T_b of 25 different planes ($N_p = 25$) over the cell size along the main fluid flow direction z. Additional planes normal to the x, y, and z axes were defined at intervals of 0.25 mm throughout the computational domain. These planes were used to extract contours of pressure, total pressure, velocity, temperature, and velocity vectors. In addition, 15 lines aligned with the z axis were defined to monitor the spatial evolution of pressure, total pressure, velocity, and temperature along the main flow direction. The exact location and a visual representation of these lines are provided in Supplementary Section S3.

The main dimensionless quantities employed to characterize the flow and heat transfer are introduced below. The Reynolds number based on the cell diameter Re_c was defined as

$$Re_c = \frac{\rho u (L_z/\varepsilon)}{\mu}, \tag{10}$$

where the cell diameter is defined as in [24]. In the cases evaluated here, it corresponds to the length of the unit cell L_z. The volumetric Nusselt number (Nu_v) is defined using the same characteristic length as:

$$Nu_v = \frac{hAV_{ratio}(L_z/\varepsilon)^2}{\lambda}. \tag{11}$$

Additionally, the Reynolds number based on the hydraulic diameter and the porosity was defined as:

$$Re_{D_h-\varepsilon} = \frac{\rho u D_h}{\mu\varepsilon}, \tag{12}$$

where the hydraulic diameter (D_h) is calculated as

$$D_h = \frac{4\,\varepsilon}{AV_{ratio}}, \tag{13}$$

and the AV_{ratio} is the ratio between the solid surface of the cell and its total volume.

Other additional useful quantities were the Hagen number [58], defined as

$$Hg = \frac{\Delta P}{\Delta L}\frac{D_h^3}{\rho\nu^2}, \tag{14}$$

the friction factor, defined as

$$f = \frac{\Delta P}{L_z}\frac{4r}{\rho\bar{u}^2}, \tag{15}$$

with r being the strut radius and $\bar{u}$ the average velocity, and the Colburn factor defined using the hydraulic diameter:

$$j_{D_h} = \frac{Nu_{D_h}}{Re_{D_h}\,Pr^{1/3}}, \tag{16}$$

with Pr being the Prandtl number. The ratio between the Colburn factor (j) and the friction factor (f) is known as the area goodness factor [13]. Here it is defined as:

$$gdn_{D_h} = j_{D_h}/f. \tag{17}$$

The pressure drop per unit length $\Delta p/L_z$ is evaluated as the difference between the average total fluid pressure at the cell inlet and outlet, divided by the cell size along the fluid flow direction. Finally, the dimensionless quantities $\widetilde{r}$, $\widetilde{l}$ and $\widetilde{AV}_{ratio}$ used in the correlations were defined as:

$$\widetilde{r} = \frac{r}{\sqrt{L_x^2 + L_y^2 + L_z^2}}, \tag{18}$$

$$\widetilde{l} = \frac{\sum_{i=1}^{n} l_i}{L_z}, \tag{19}$$

$$\widetilde{AV}_{ratio} = \frac{A_{sf}}{V_{tot}^{2/3}}, \tag{20}$$

being L_x, L_y and L_z the dimensions of the cell in the three directions. All the previous quantities were obtained from the Ansys CFD-Post software. Further details are provided in the Supplementary Section S4. The dedicated protocols and Python scripts are also provided in the Supplementary Data file.

2.6. Regression on the results

The results of the simulations were analyzed by means of Symbolic Regression (SR), in order to obtain closed-form analytical expressions for the target performance metrics as a function of relevant cell descriptors. In this view, SR is particularly useful because it enables expressions based on interpretable descriptors to be obtained directly from an available dataset [59]. Unlike traditional methods, where regression relies on predefined equation templates, SR enables the identification of complex, non-linear relationships that would be otherwise very difficult to discover [60].

Here, HeuristicLab [61], an open-source optimization environment that implements SR using Genetic Programming (GP), was employed. This approach enables candidate mathematical expressions to be evolved to model target variables from the input data. Each candidate model is represented as a tree structure, where the internal nodes correspond to mathematical operators (such as addition, multiplication or trigonometric functions), and leaf nodes represent input variables or constants. The GP algorithm iteratively refines these trees through genetic operations, such as mutation and crossover, guided by a function that quantifies the prediction error of the model. In order to balance accuracy and complexity, constraints on tree depth (max number of hierarchical levels) and tree length (the total number of nodes) are typically enforced during evolution. This allows the discovery of compact, closed-form expressions that capture latent relationships in the data.

In the present study, the goodness of each candidate expression was evaluated based on its ability to accurately fit the simulation data, focusing specifically on minimizing the errors with respect to geometric descriptors of the cells and flow-related parameters (e.g. the Reynolds and Nusselt numbers). The analysis started with the generation of an initial set of candidate fitting equations. Each expression was then evaluated based on fitness functions that, in this case, were the Root Mean Square (Percentage) Error (RMSE) and the Average Relative Error (ARE) between the predicted values ($y_{m,i}$) and the simulation data (y_i), namely

$$\mathrm{RMSE} = \sqrt{\frac{1}{n}\sum_{i=1}^{n}\left(\frac{y_{m,i} - y_i}{y_i}\right)^2}, \tag{21}$$

and

$$\mathrm{ARE} = \frac{1}{n}\sum_{i=1}^{n}\left|\frac{y_{m,i} - y_i}{y_i}\right|. \tag{22}$$

The best candidate expressions were then improved further using genetic operators, such as mutation and crossover, to introduce variations in the equations and to combine the most performing features from different candidate expressions. This evolutionary process was repeated several times (generations), to progressively improve the accuracy and the simplicity of the final fitting equations.

For the analysis, the generated dataset was reduced from the overall 540 simulations to remove some outliers: the max pressure drop per unit length was set to 9000 Pa/m. These high-pressure-drop configurations were not considered non-physical; rather, they were treated as outside the intended validity range of the proposed correlations, which are aimed at open-cell configurations without severe inlet blockage.

Simulations that did not reach a continuity residual below 10^{-4} were also discarded. Based on these criteria, the final dataset included 397 simulations. All input variables were derived from the geometrical features of the cell and from the fluid-dynamic and thermal operating conditions, ensuring that all descriptors retain a clear physical meaning within the framework of porous media modeling. In particular, the selected descriptors were formulated in terms of dimensionless groups and geometrically meaningful quantities, while avoiding redundancy and multicollinearity among variables. For this reason, mutually dependent quantities were not used simultaneously (e.g., porosity was not included as an independent variable when the hydraulic diameter was adopted). The full dataset was then shuffled and split into a training set (66%) and a test set (34%). Symbolic regression was performed using a population of 1000 candidate equations evolved over 500 generations, retaining the two best-performing individuals at each generation (elitism). The mutation probability was set to 15%, crossover was implemented through subtree swapping, and tournament selection was adopted [62]. To increase interpretability and limit model complexity, the maximum tree depth and tree length were constrained (typically up to 8 levels and 40 nodes), and the final expressions were further reduced using the "Simplify Model" function.

3. Results and discussion

3.1. Model validation

Upon identification of the correct numerical set-up that guarantees independence of the solution from domain discretization and size of the control volume, the simulations were validated against simulation and experimental data available in the literature. Particularly, the results obtained for the Cube, FD-Cube and Octet geometries were compared with the simulation data in [25]. In that work, flow and thermal transport was analyzed across one grid with infinite extension in the directions perpendicular to the flow, and with a length of one cell in the direction of the flow. Four different unit cell geometries, with a porosity of 0.986, and at 5 different inlet flow speeds (from 0.5 to 2.3 m/s) were simulated. The 4 cells were the Cube, the FD-Cube, the Octet and the Tetrakaidecahedron (TKD); however, while the first three had struts with a circular cross section as in the present work, the TKD structure had the fiber with a tricuspid shape. Consequently, the results obtained here were only compared with the correlations obtained for cells with the fibers with a circular cross-section. The correlations were in the form [25]

$$Nu_v = a Re_c^b Pr^{0.4}, \tag{23}$$

where a and b are two coefficients based on the cell topology, Re_c is the Reynolds number based on the cell diameter and Nu_v is the volumetric Nusselt number.

The geometric coefficients a and b used in Eq. (23) were: 3.1733 and 0.3168 for the Cube cell, 4.7926 and 0.3566 for the FD-Cube cell, 9.3982 and 0.3926 for the Octet cell [25]. The results are shown in Fig. 4. The errors obtained for the Cube, the FD-Cube and Octet geometries were 2.5%, −6.8% and 6.5% respectively.

Kelvin cells are largely used to model random foams [24], so the results for this specific geometry were validated by comparing them to semi-empirical correlations for pressure drop developed for single-phase flow in open cell ceramic sponges [58]. The same correlation was then validated using a large dataset of experimental values for flow through both metal and ceramic sponges [23]. The equation is valid for a wide range of Reynolds numbers $Re_{D_h-\varepsilon}$ (between 10^{-1} and 10^5). The dimensional correlation was based on Ergun type equations, and it can be written as

$$\frac{\Delta P}{\Delta L} = 110 \frac{\mu}{\varepsilon D_h^2} u + 1.45 \frac{\rho}{\varepsilon^2 D_h} u^2. \tag{24}$$

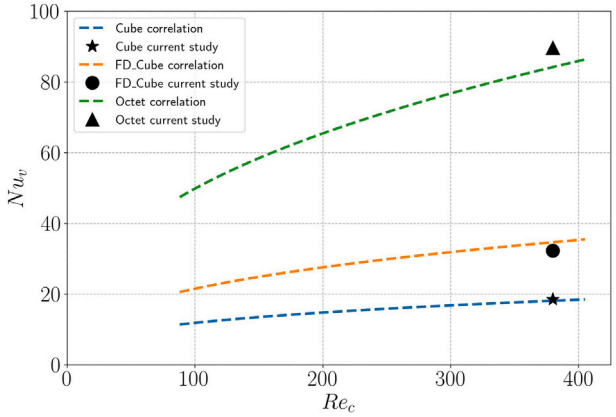


Fig. 4. Comparison of the volumetric Nusselt number obtained in the current study for different cells with the correlations reported in [25].

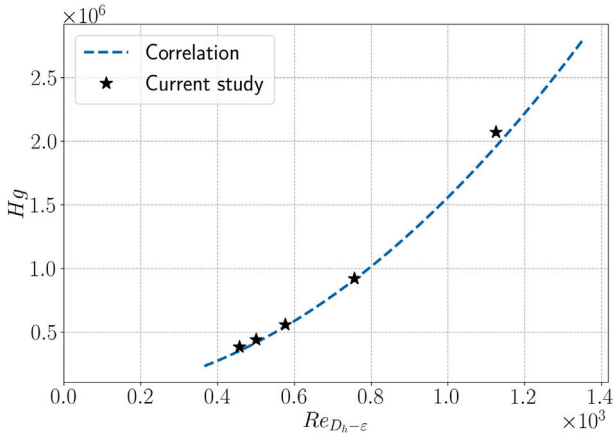


Fig. 5. Comparison of the Hagen numbers obtained in the current study for a Kelvin cell (with 1.0 elongation along the flow direction and porosity values in the range 0.83 to 0.981) and the correlation in Eq. (25), developed by [58].

Using the definition of the Reynolds number in Eq. (12), and of the Hagen number [58] defined in Eq. (14), Eq. (24) can be recast in dimensionless form as [58]

$$Hg = 110\, Re_{D_h-\varepsilon} + 1.45\, Re^2_{D_h-\varepsilon}. \tag{25}$$

This latter function is shown in Fig. 5, along with the values obtained in the current study for a Kelvin cell with an elongation of 1.0 along the flow direction and porosity values in the range 0.83 to 0.981. The relative errors for the Hagen number Hg for the five simulations were calculated to be between 1% and 8% with respect to the correlation.

Figs. 4 and 5 together provide a complementary validation: Fig. 4 accounts for geometric features at a representative working condition, while Fig. 5 accounts for the effect of Reynolds number within the considered range.

For the sake of completeness, the results obtained for Kelvin and Diamond cells were also compared with the correlations developed by [63], based on both simulation and experimental data. The errors obtained between the simulations and the correlation were: 0.2%, 12% and 20% for porosity values of 0.91, 0.87 and 0.84 for a Kelvin cell and 2%, 18% and 31% for porosities of 0.91, 0.87 and 0.84 for a Diamond cell. The details of this latter comparison are reported in the Supplementary Section S5.

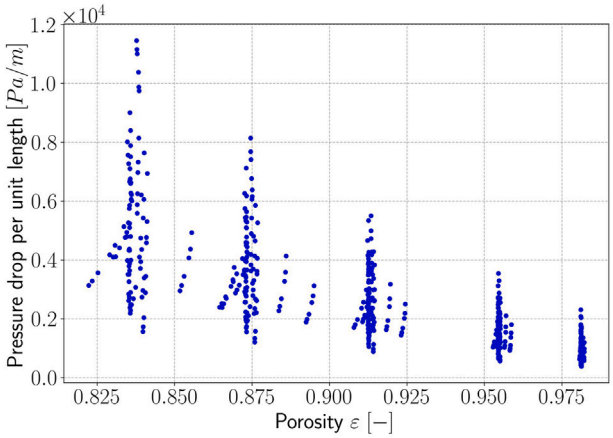


Fig. 6. Pressure drop per unit length as a function of the porosity ε (without the Hexagonal_GEO geometry).

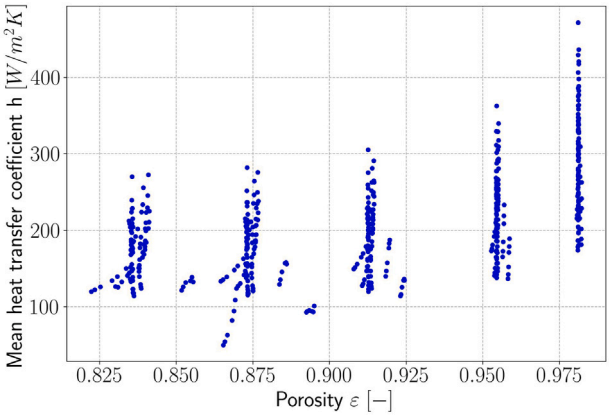


Fig. 7. Mean heat transfer coefficient as a function of the porosity ε.

3.2. Raw results

While examining the results on the computed pressure drop per unit length for all the considered cases, it was found that the hexagonal cells in the lowest porosity range, that is 0.8-0.9, exhibited a significant deviation compared to the other cells (see Figure S20). These large deviations can be attributed to the vast portion of the inlet region of the cell occupied by solid volume, which leaves only some small gaps for the fluid to pass through. The same geometry with porosity $\varepsilon = 0.98$ is shown in Fig. 1(r). The significant deviation with respect to all the other topologies led us to exclude these values from the dataset. The cleaned dataset is shown in Fig. 6. The pressure drop per unit length shows a decreasing trend with increasing porosity, as the cells with higher porosity have struts with smaller radius and thus smaller recirculation zones. The friction factor, defined in Eq. (15) follows a similar trend to that of the pressure drop per unit length as expected, since it is by definition linearly dependent on the pressure drop. For completeness, the friction factor f as a function of the porosity ε is shown in Figure S21. Note that, in general, well-established classical porous-media closures such as Carman-Kozeny and Darcy-Forchheimer [64] provide elegant representations of permeability and inertial losses for random porous media. However, for ordered lattice cells, pressure losses depend strongly on topological features (e.g., ligament arrangement), which cannot be accurately captured by the porosity only. For this reason, here the solutions are not constrained to target equation templates.

The mean heat transfer coefficient was found to be less dependent on the porosity compared to the pressure drop per unit length (see Fig. 7). The wide range of mean heat transfer coefficient per given porosity, especially for the highest porosity values, suggests that other topological factors influence the parameter on the y-axis. For example, the surface area of the solid volume of the cell has a clearer influence on the mean heat transfer coefficient h, as shown in Figure S22. The mean heat transfer coefficient decreases as the surface area increases. Under the imposed heat flux conditions indeed, a larger surface area implies an increase in the heat transfer rate; however, in steady laminar flow, additional surface can be also associated with sheltered low-velocity regions and thicker thermal boundary layers, which may ultimately induce a reduction of the heat transfer coefficient. Therefore, this trend can be partially explained by the fact that the heat transfer coefficient becomes lower as the cell elongation along the flow direction increases, as also found in [34].

The Colburn factor defined in Eq. (16) decreases as the surface area of the cell increases, as shown in Figure S23. The trend is similar to that observed for the heat transfer coefficient, and can be partially explained by the decrease in the Colburn factor associated with an increase in the elongation of the cell along the flow direction, in accordance with the results in [34]. The highest values for the Colburn factor were obtained for the highest values of porosity.

The area goodness factor, defined as the ratio (j/f) between the Colburn factor and the friction factor (see Eq. (17)), decreases as the dimensionless surface-to-volume ratio, defined in Eq. (20), increases. The data are shown in Figure S24. It can be observed that the inverse dependence is stronger compared to the previous plots. The highest values of the goodness factor were obtained for the cells with the highest porosity: in particular all the values above 1.5 are obtained from cells with porosity greater than 0.97.

Finally the relations between Nusselt number and Reynolds number were different depending on whether the dimensionless quantities were based on the hydraulic diameter or on the strut diameter as characteristic length. In the first case, plotted in Figure S25, the volumetric Nusselt number decreases as the Reynolds number based on the hydraulic diameter increases. However, when the same Nusselt number is plotted against the Reynolds number based on the cell length and the porosity for a specific cell, it is found that the Nusselt number increases as the Reynolds number increases for a specific geometry, as shown in Figure S26. This is in accordance with [25,65].

Finally, the relation between the Nusselt and the Reynolds number which use the strut diameter d as characteristic length is shown in Figure S27. In this case the Nusselt number Nu_d increases as the Reynolds number Re_d increases.

3.3. Flow analysis: physical insights

In order to gain physical insight into the fluid-dynamic reasons for the results obtained on pressure drop and heat transfer, a representative set of simulations for all the considered geometries ($z_f = 1.0$ and $\varepsilon = 0.98$, see Table S4) was examined in detail.

To ease the comparison of different cells, a custom Graphical User Interface (GUI) program was developed in Python. The tool allows to compare the relevant quantities and the flow structures around different topologies (see Supplementary Section S6), thus allowing to appreciate e.g. the different velocity distributions for the different geometries.

The cells with the lowest pressure drop were the Cube, the Body center and the Diamond. The first one had the ligaments concentrated around the border of the unit cell, allowing the flow to pass in the middle without obstacles, while the other two cells had no ligament perpendicular to the flow direction. Thanks to the angle between the flow direction and the ligament, the section seen by the flow was not circular, but elliptical. This has multiple effects on the flow. The body behaves as a streamlined geometry. In laminar cross-flow conditions, this configuration reduces the adverse pressure gradient along

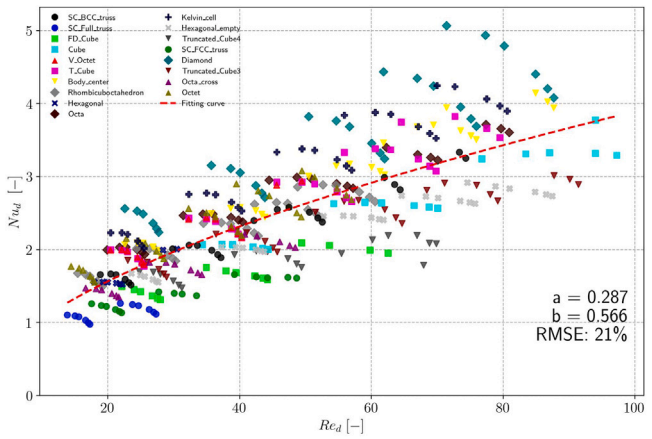


Fig. 8. Results of the 397 simulations in the final dataset, and best fitting curve according to Eq. (26). The obtained values of the fitting parameters are also reported, along with the RMSE error.

the surface which in turn delays boundary-layer separation, leading to a narrower wake region compared to a circular cylinder. As a consequence, both the pressure drag and the associated friction factor are significantly reduced. These results are consistent with previous studies [34,66]. The cells in which the struts were not in the wakes of other ligaments, on the other hand, achieved the highest heat transfer coefficient h. These geometries were the Kelvin cell, the Octet, the Diamond and the Rhombicuboctahedron. Thanks to these characteristics, the Diamond and the Body center had the largest goodness factors, followed by the Rhombicuboctahedron, the Kelvin, the Octa and the Octet cells.

3.4. Correlation equations

The data obtained from the simulations were used to generate different correlation equations based on the quantities of interest. A simple correlation was first developed using the curve fitting function of the SciPy Python package [67]. A set of more complex equations were then derived using Symbolic Regression (see Section 2.6).

The simplest versions of the correlation equations were based on the equations of the type

$$Nu_d = a\, Re_d^b, \tag{26}$$

where Nu_d and Re_d are the Nusselt number and the Reynolds number based on the ligament diameter respectively, while a and b are two coefficients. These latter coefficients were best-fitted on all the 397 simulations of the final dataset, with RMSE and ARE equal to 21% and 16.3%, respectively. The fitting curve along with the raw data are shown in Fig. 8.

The cleaned dataset included multiple types of cells with 20 or more simulations, which were used to calculate the specific coefficients for a certain type of geometry (the detailed results are reported in the Supplementary Table S5). The observed spreading of data is then expected, and can be related to topology-dependent effects. For all cases, the Nusselt number was found to be proportional to $Re^{0.566}$. The exponent close to 0.5 is consistent with the findings in [32], where a relation of the type $Nu = Re^{0.5}$ for $Re_d > 2$ or $Re_{D_h} > 30$ was proposed. The observed scaling $Nu \propto Re^{0.5}$ can be interpreted in terms of laminar boundary-layer theory, where the thermal boundary-layer thickness scales as $\delta_t \propto Re^{-0.5}$ when $Pr = O(1)$. Consequently, the heat transfer coefficient scales as $h \propto k/\delta_t \propto Re^{0.5}$, leading to the observed Nusselt number dependence. The errors for the equations of this type are between 4% and 10%. The correlation for the Hexagonal-empty geometry provided the best approximation of the simulation results, while that for the Diamond cell was the least accurate. Supporting plots for the topology-specific power-law fits are reported in Supplementary Figures S18 and S19.

Symbolic Regression was then used to explore a larger set of equations, and to find the parameters with the largest influence on the investigated quantities. All the sets (combinations) of input variables, directly or indirectly, included all the *basic* geometric variables. The final correlations shown in this section were derived through a multi-step process (see also Section 2.6), where the initial trials were conducted with a tree length around 150, and a large number of independent variables, resulting in very complex expressions. After the first runs, the input variables with a negligible impact (less than 5% influence on the final result) were discarded from the set. The parameters as well as the variables were then progressively reduced and simplified, to obtain a final correlation that depended on a maximum of 4 or 5 variables and with a tree length below 40.

At the end of the process, the only variables that were found to have an influence on the target quantities were: the z_factor, *i.e.* the ratio between the length of the cell along the flow direction and the width of the cell; the porosity (ε), defined as the volume of void over the total volume of the cell; the AV_{ratio} and its dimensionless counterpart $\widetilde{AV}_{ratio}$, *i.e.* the ratios between the surface of the solid volume and the total volume of the cell; the dimensionless radius $\widetilde{r}$, *i.e.* the radius of the ligaments divided by the cell diagonal to make it dimensionless; $\widetilde{l}$, i.e. the total length of the ligaments divided by the length of the cell; D_h, the hydraulic diameter. For the definition of all these quantities, see Section 2.5 and Supplementary Section S4.

Clearly, these variables were selected as a possible minimal set of effective descriptors for the problem under investigation. Additional variables extracted during the CFD post-processing phase were also evaluated, but were found to have a negligible influence on the target quantities. These were: the mean angle between the flow and the struts; all the ratios between the ligaments at certain angles and the total length of the ligaments; the length of the projection of the ligaments on the frontal area of the cell divided by the diagonal of the frontal area; the percentage of frontal area covered by the ligaments.

Based on the selected set of variables, the following derived equations were chosen as the most promising in terms of simplicity and accuracy: one equation for the Nusselt number as a function of the Reynolds number; one equation for the friction factor as a function of the Reynolds number; one equation for the area goodness factor. In addition to the correlations presented in this section, several alternative symbolic regression models were also explored using different combinations of input variables. Although these models provided useful insights, they exhibited lower predictive performance and were therefore not retained in the main discussion. Their corresponding equations and validation results are reported in the Supplementary Section S7.

For each equation presented below, statistical indicators are reported to assess predictive accuracy, including the Average Relative Error (ARE) and the coefficient of determination (R^2), evaluated on both training and test datasets. In addition, a variable importance measure, referred to as Variable Impact, is provided. This metric is computed within the HeuristicLab framework using a permutation-based sensitivity analysis. Specifically, the predictive model is first evaluated on the original test dataset to establish a baseline performance. Subsequently, each input variable is individually perturbed by randomly permuting its values across the dataset, while keeping all other variables unchanged. This procedure breaks the statistical relationship between the selected variable and the target output without altering its marginal distribution. The model is then re-evaluated on the test set, and the resulting degradation in predictive performance is used to quantify the relative importance of that variable. A higher Variable Impact value indicates a stronger contribution of the corresponding parameter to the model output.

$$Nu_{D_h} = \frac{0.39969 \cdot Re_{D_h}}{\left(2.7425 \cdot \widetilde{l} + 17.853\right)\left(4.1912 \cdot \widetilde{r} \cdot z_f + Re_{D_h} \cdot 2.2021 \times 10^{-5}\right)} + 10.316 \tag{27}$$

Eq. (27) can be used to calculate the Nusselt number Nu_{D_h} based on the Reynolds number Re_{D_h}, the dimensionless radius $\widetilde{r}$, the cell elongation ratio z_f and the dimensionless length $\widetilde{l}$. In this case, the ARE for the training and the test sets were 11.67% and 12.25% respectively with corresponding coefficients of determination of $R^2 = 0.923$ and $R^2 = 0.906$. The variables exhibiting the highest Variable Impact on the target response were the dimensionless radius ($\widetilde{r}$) and the Reynolds number based on the hydraulic diameter (Re_{D_h}), with values of 0.59 and 0.51, respectively. The z-factor (z_f) and the dimensionless length ($\widetilde{l}$) showed a comparatively lower influence, with Variable Impact values of 0.41 and 0.24, respectively.

The equation for the friction factor f relies on the Reynolds number based on the hydraulic diameter Re_{D_h}, the dimensionless radius $\widetilde{r}$, the z_factor z_f and the dimensionless length $\widetilde{l}$ as:

$$f = \frac{3.6333 \times 10^3 \cdot \widetilde{r}}{0.61142 \cdot Re_{D_h} + A_1 - B_1 - 27.121} - 4.9804 \times 10^{-3} \tag{28}$$

with

$$A_1 = \frac{1}{1.8938 \times 10^{-2} \cdot \widetilde{l} \cdot \widetilde{r}} \tag{29}$$

$$B_1 = 0.55227 \cdot \left(Re_{D_h} \cdot \widetilde{r} \cdot z_f \cdot \left(1.4113 \cdot z_f + \widetilde{l} \cdot 0.21407\right)\right) \tag{30}$$

The regression achieved an ARE of 8.98% for the training set and 10.6% for the test set, with corresponding coefficients of determination of $R^2 = 0.979$ and $R^2 = 0.971$, respectively. For this correlation, the Variable Impact analysis indicated that the dimensionless ratio ($\widetilde{r}$) was the most influential parameter, with a value of 0.917. The Reynolds number based on the hydraulic diameter (Re_{D_h}) showed a secondary but still relevant contribution (0.311), followed by the elongation along the flow direction (z_f) (0.244). The dimensionless length ($\widetilde{l}$) exhibited the lowest impact on the model output, with a value of 0.140, indicating a comparatively minor role within the investigated range.

It can be observed that the friction factor scales as $f \propto 1/Re_{D_h}$, which is consistent with the Darcy's regime, where viscous forces dominate the pressure drop. In this regime, the pressure drop is proportional to the superficial velocity, resulting in the inverse dependence of the friction factor on Reynolds number.

The equation for the goodness factor was more complicated, and involved a higher number of variables. It relates the goodness factor gdn_{D_h} with the Nu_{D_h}, the $\widetilde{r}$, the $\widetilde{l}$, the z_f, the $\widetilde{AV}_{ratio}$ and the porosity of the cell ε. It yields as

$$gdn_{D_h} = -0.0041074 \cdot Nu_{D_h} + \left(6.0907 \times 10^{-4} \cdot \widetilde{r}\right) + \\ + A_4 - B_4 + 0.0052336 \tag{31}$$

with

$$A_4 = \frac{Nu_{D_h} \cdot (0.34805 \cdot \widetilde{l} + 2.009 \cdot \varepsilon) \cdot 4.4903 \times 10^{-4}}{0.54135 \cdot \widetilde{l} \cdot \widetilde{r}} \tag{32}$$

$$B_4 = \frac{3.5679 \times 10^{-4} \cdot Nu_{D_h} \cdot z_f}{1.2692 \cdot \widetilde{r} \cdot \left(0.34746 \cdot z_f + 2.238 \cdot \widetilde{AV}_{ratio}\right)} \tag{33}$$

The errors obtained in this case were 11.47% and 9.69% for the training and test sets, respectively. Similarly, the coefficients of determination were $R^2 = 0.964$ for the training and $R^2 = 0.981$ for the test set. In this case, the Variable Impact analysis indicated that the most influential parameters were Nu_{D_h} and $\widetilde{r}$, with impact values of 0.781 and 0.737, respectively. The dimensionless length $\widetilde{l}$ showed a moderate influence (0.206), while the remaining parameters, including the z_f and the dimensionless area-to-volume ratio $\widetilde{AV}_{ratio}$, exhibited a progressively lower contribution (0.035 and 0.032, respectively). The porosity ε had a negligible impact (0.003), indicating a marginal role within the regression model.

As previously done for the simple correlation equation at the beginning of this section, specific equations for the Nusselt numbers Nu_{D_h} and Nu_d as a function of the Reynolds numbers Re_{D_h} and Re_d were also derived. These equations are reported in the Supplementary Section S8.

Please note that, while the present symbolic-regression models were derived as analytical expressions based on flow and geometric descriptors, further improvement towards mechanistic interpretability is possible. One possible way could be to consider different physically-ground descriptors (e.g. for flow separation or wake interaction) for the regression. Another possibility could be to constrain the search space of the correlations using physically-motivated equation templates (e.g., viscous-inertial decomposition for pressure losses, or boundary-layer based scaling for heat transfer), allowing the regression to identify geometry-dependent coefficients within predefined mechanistic forms. As an example, the generated dataset could be used to formulate a Darcy-Forchheimer type equation [64], where the effective permeability and inertial coefficients can be correlated to geometric descriptors using symbolic regression, thus providing a direct link between the cell topology and classical porous-media modeling frameworks.

3.5. Correlation assessment

The correlations presented in the previous section were assessed against independent datasets corresponding to cell topologies that were not included in the symbolic regression training dataset. Since the proposed models were developed using a numerical database representative of open-cell metal foams with pore densities close to 10 PPI, the validation was restricted to literature data within the same geometrical range. This approach provides an initial assessment of the generalization capability of the correlations for previously unseen geometries within their intended domain of applicability.

The three geometries used were the Weaire–Phelan structure from [68], the modified Kelvin cell from [34] and the tetrahedral cell from [36]. The data from the first study were obtained through simulations, while the last one includes both simulations and experimental measurements. The first structure consists of two types of cells: the Dodecahedron and the Tetrakaidecahedron. The two different geometries are connected in a ratio of three tetrakaidecahedron cells for each dodecahedron cell. This geometry is also a good approximation to model real random foams [68]. The modified Kelvin cell is a Kelvin cell where the windows perpendicular to the flow direction are larger to enhance the overall performance of the cell. The measure used to characterize the cell was the diagonal of the window perpendicular to the flow direction. In the study, two variations of the basic Kelvin cell are used: one has the diagonal equal to 1.3 times the base one and the other equal to 1.5. The tetrahedral cell was a pyramid structure with all faces being equal.

In Fig. 9(a) it is possible to see the accuracy of correlation (28) for Tetrahedral cells with both experimental and simulation data. Most of the considered points fall within the ±40% deviation band for cells with porosity from $\varepsilon = 0.75$ to $\varepsilon = 0.90$ and in laminar regime. The correlations proposed by Calmidi [69] and Dukhan [70] were not included in this comparison because they were developed for open-cell metal foams described through foam-scale parameters such as porosity and pore density, whereas the Tetrahedral cells considered here are ordered lattice structures with a substantially different topology.

In Fig. 9(b), the correlation is able to reasonably predict the friction factor for the modified Kelvin cell and for some points of the Weaire–Phelan structure at 10 pores per inch, together with the correlations proposed by Calmidi [69] and Dukhan [70]. The proposed correlation gives predictions comparable to the Calmidi correlation for the 10 PPI Weaire–Phelan data. For the modified Kelvin data, the proposed correlation provides estimates comparable to those obtained

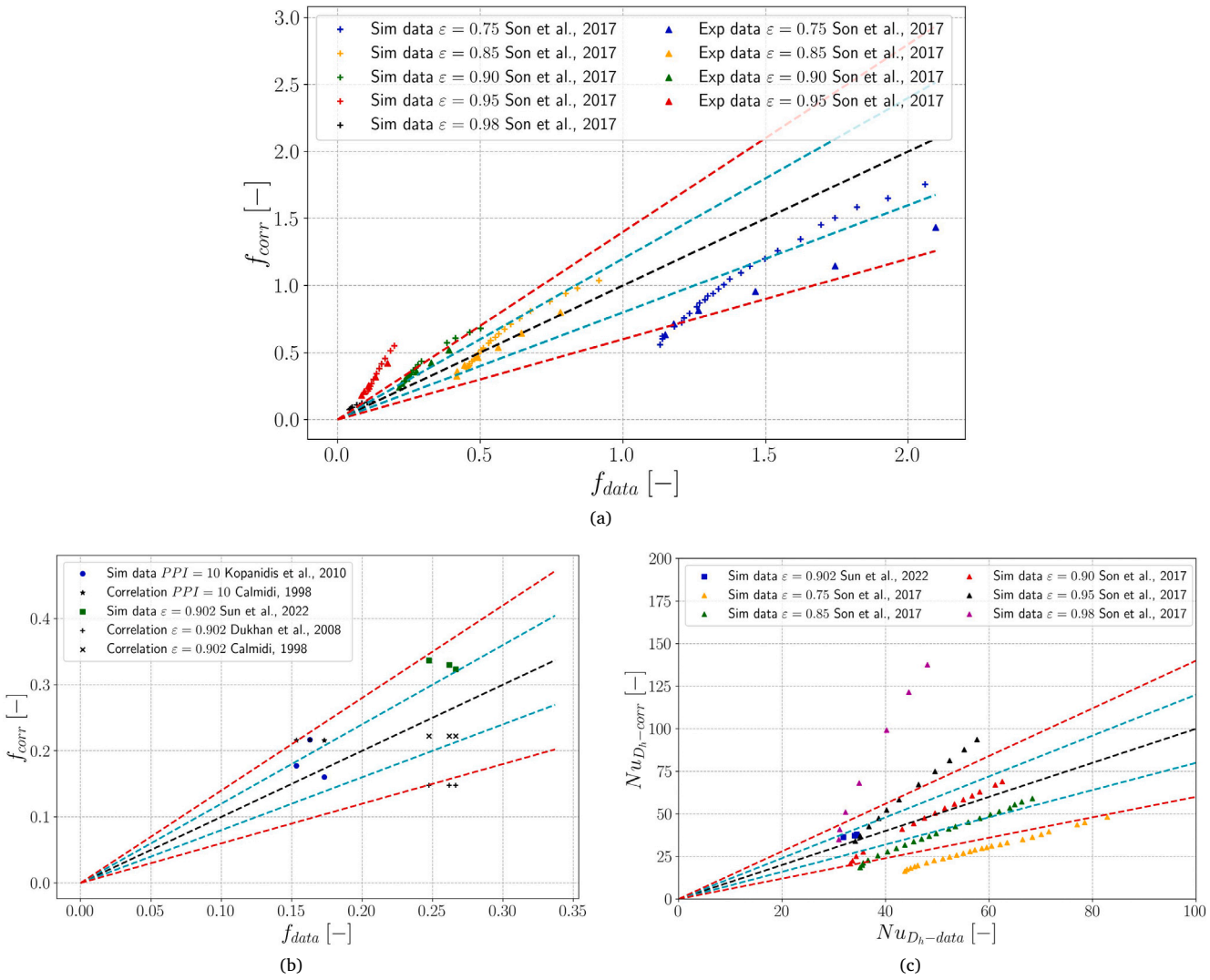


Fig. 9. (a) Correlation (28) compared with experimental and simulated data from [36]; (b) Correlation (28) compared with simulation of a modified Kelvin cell [34], a Weaire–Phelan structure [68] and correlations from Calmidi [69] and Dukhan [70]; (c) Correlation (27) compared with Tetrahedral (triangular markers) and modified Kelvin cells (square markers). The black dashed lines correspond to the correlation line, the light-blue dashed lines to ±20% error, and the red dashed lines to ±40% error.

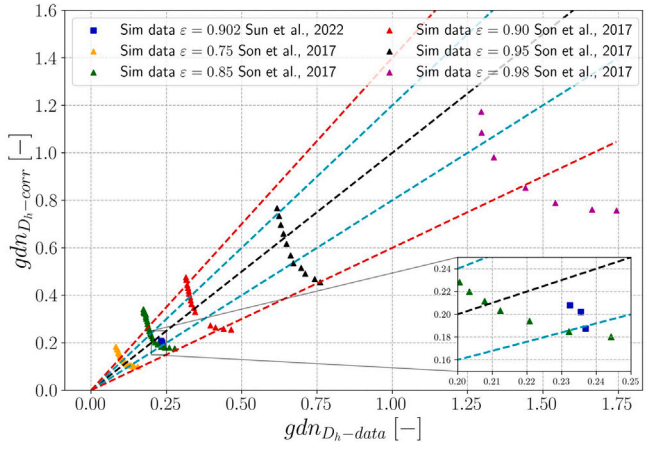


Fig. 10. Correlation (31) used with modified Kelvin cells (square markers, Sun et al. 2022) and with Tetrahedral cells (triangular markers, Son et al. 2017). The black dashed lines correspond to the correlation line, the light-blue dashed lines to ±20% error, and the red dashed lines to ±40% error.

with the Calmidi and Dukhan correlations. This comparison suggests that Eq. (28) retains reasonable predictive capability for unseen Kelvin-like and Weaire–Phelan geometries, although within the limits of the laminar and geometrical range considered in this work.

Correlation (27) was compared with the studies in which the heat transfer data were available. The results are shown in Fig. 9(c). The predicted results generally fall within a ±40% deviation band for the modified Kelvin cells and for the Tetrahedral cells within the range of porosity 0.85-0.95, which is considered suitable for preliminary engineering estimates within the intended validity range.

Fig. 10 compares the predicted values of the goodness factor given by Eq. (31) with the data for the modified Kelvin cells (Sun et al. 2022) and for the Tetrahedral cells (Son et al. 2017). For the modified Kelvin cells, most deviations remain within the ±20% band; on the other hand, for the Tetrahedral cells the errors can be larger.

In general, the best performance of the proposed correlations is found for laminar conditions and porosity between 0.8 and 0.95 in most cases, whereas a larger scatter is observed outside this range and for different geometries. In such cases, larger errors can be expected, and

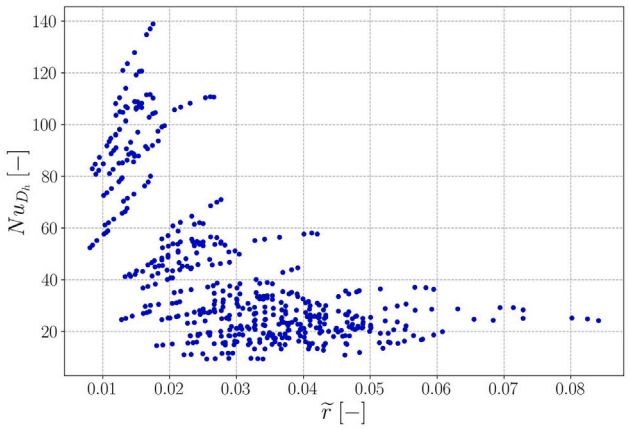


Fig. 11. Nu_{D_h} as a function of the dimensionless radius $\tilde{r}$.

reflect the balance between the current model generality and predictive accuracy.

3.6. Discussion of the equations

Eq. (26) shows a relation of the type $Nu = aRe^b$, where the b coefficient (on a per-geometry basis) was in the range 0.426 – 0.575. In a similar correlation found by [25], shown in Eq. (23), the coefficient of the Reynolds exponent was in the range 0.3382 – 0.4001, as shown in Section 3.1. The main difference is that the aforementioned authors used the volumetric Nusselt number and the Reynolds number based on the cell dimension instead of the dimensionless quantities based on the ligament diameter. Despite that, the trend of the two correlations is similar, with exponents in a similar range.

In Eq. (28), for a fixed cell geometry, the friction factor exhibits an approximately inverse scaling with Re_{D_h} which is consistent with the characteristic $\sim 1/Re$ in laminar flows. However, the complexity of the cell introduces additional geometric parameters, such as $\tilde{r}$, $\tilde{l}$ and z_f, which act as topological correction factors.

In Eq. (27), the strongest effect on the Nusselt number can be attributed to the term $\tilde{r}\, z_f$. The strong dependence of the Nusselt number on the dimensionless radius $\tilde{r}$ is clearly visible in Fig. 11, whereas the dependence on the cell elongation z_f (not shown) was found to be smaller. Unlike conventional empirical correlations, the symbolic regression framework automatically identified the relative importance of the geometric descriptors without prescribing a functional form a priori. In particular, the recurrent appearance of the dimensionless ligament radius $\tilde{r}$ in the derived expressions indicates that this parameter plays a dominant role in determining both the hydraulic and thermal performance of the investigated unit cells. This suggests that the ratio between ligament radius and the cell dimension should be regarded as a primary design variable during the optimization of additively manufactured metal foams.

The equation for the goodness factors (31) also shows a diminishing trend for increasing values of the dimensionless radius. The goodness factor increases as the elongation factor z_f increases, as also found by [34] in their studies.

In all the equations derived for specific cells, namely from equation S21 to equation S40, the two parameters that have the largest effects on the target variables are the Reynolds numbers and the cell elongation ratio. In the equations where both the Nusselt number and the Reynolds number use the hydraulic diameter as characteristic length, the majority of the correlations include a dominant term $Nu_{D_h} \sim Re^2_{D_h}/(c_1\, z_f + c_2)$ and, a few more, terms in the form $Nu_{D_h} \sim Re^2_{D_h}/e^{c_3\, z_f}$ (with c_1, c_2 and c_3 indicating here generic constants). The hydraulic diameter was defined accordingly to Eq. (13), so the cells with the largest AV_{ratio}, which were the ones with the largest porosity ε, had the smallest hydraulic diameter. Overall, the correlations capture the expected increase of the Nusselt number with the Reynolds number. Regarding the correlation with both Nusselt number and Reynolds number based on the ligament diameter instead, only a subset of them included terms in the form $Nu_d \sim Re_d/(c_1\, z_f + c_2)$ or $Nu_d \sim Re_d/e^{c_3 z_f}$, whereas others showed more complex combinations of Re_d, z_f, and ε. In conclusion, while the heat transfer–pressure drop trade-off is well established, the present work extends this analysis to additively manufactured open-cell geometries through data-driven symbolic regression models. Unlike conventional regression approaches based on predefined functional forms, the proposed methodology provides explicit analytical expressions that directly quantify the influence of the main geometric descriptors, thereby offering practical guidance for geometry selection during the preliminary design of heat exchangers based on open-cell metal foams.

4. Conclusions

The effect of different unit cell geometries on the heat transfer and pressure drop characteristics in metal foams for heat exchangers was analyzed.

A large dataset with the thermal-fluid dynamics characteristics of a wide range of unit cell geometries was created. Particularly, 18 different unit cell geometries with 5 different porosity values and 6 elongations along the principal flow direction were simulated, for a total of 540 different cases. The flow pattern inside the cells was analyzed, to understand which features influence the thermo-fluid dynamic performance of the cells. The ligament radius as well as the angle between the ligaments and the flow direction significantly impacted the heat transfer and the pressure drop inside the cell. Thick ligaments created large recirculation zones, which increased the pressure losses and decreased the heat exchange between the fluid and the cell struts.

Then, a set of correlation equations between fluid dynamics parameters and geometric parameters were derived using symbolic regression. The developed correlations were assessed against three structured-foam geometries that were not included in the initial dataset. The topology of the cells has been found to play an important role in both heat transfer and pressure drop characteristics.

When compared with selected literature datasets within the intended laminar and geometrical range of applicability, Eq. (28) generally predicted the friction factor within a ±40% deviation band. For the Nusselt number, two different equations were derived: a complex correlation where the Nusselt number was based on the hydraulic diameter (Eq. (27)) was found to be more precise than a simpler correlation of the type $Nu_d = aRe^b$ (shown in Eq. (26)). For the area goodness factor, the correlation (31) provided predictions within ±20% for the modified Kelvin cell and ±40% for the Tetrahedral cell. Finally, specific equations for the Nusselt numbers as a function of the Reynolds numbers were also derived for each cell geometry.

In summary, symbolic regression powered by genetic programming was shown to be a useful tool for developing explicit thermo-hydraulic correlations. Here the analysis was conducted for laminar flow conditions and assuming air as the heat transfer fluid. Although the correlations have been formulated using dimensionless arguments, the extension to other fluids with substantially different Prandtl number or with strong property variations (e.g., liquids or supercritical CO_2) requires potential inclusion of explicit Pr- and/or property-ratio terms, along with an augmented training dataset to calibrate the correlation coefficients. Therefore, future work could focus on extending the training dataset to a wider range of operating conditions, including transitional and turbulent flow regimes and different working fluids. It could also include additional geometrical features (e.g., non-circular ligament shapes) or fabrication-induced imperfections, in order to further improve both the predictive accuracy and the applicability range

of the proposed equations. Finally, incorporating additional descriptors could enrich the geometrical characterization and enhance the capability of the correlations to capture topology-specific effects.

CRediT authorship contribution statement

Fabio Catalano: Writing – original draft, Visualization, Validation, Software, Resources, Methodology, Investigation, Formal analysis, Data curation, Conceptualization. **Andrea Ferrero:** Validation, Supervision, Methodology, Investigation, Conceptualization. **Matteo Fasano:** Validation, Supervision, Methodology, Investigation, Conceptualization. **Luca Bergamasco:** Writing – review & editing, Validation, Supervision, Project administration, Methodology, Investigation, Conceptualization.

Declaration of competing interest

The authors declare that they have no known competing financial interests or personal relationships that could have appeared to influence the work reported in this paper.

Acknowledgments

The authors acknowledge fruitful discussions carried out within the framework of the project AMHPHEX - Additive Manufactured High-Performance Heat Exchangers.

Supplementary Information

Supplementary material related to this article can be found online at https://doi.org/10.1016/j.icheatmasstransfer.2026.112629.

Data availability

This article has an associated Supplementary Data file containing the data and scripts used in the article. The data file can be downloaded at: https://doi.org/10.5281/zenodo.18428937.

References

[1] Tian Xiao, Liu Lu, Wenhao Peng, Zengshen Yue, Xiaohu Yang, Tian Jian Lu, Bengt Sundén, Numerical study of heat transfer and load-bearing performances of corrugated sandwich structure with open-cell metal foam, Int. J. Heat Mass Transfer 215 (2023) 124517.
[2] Henk Huisseune, Sven De Schampheleire, Bernd Ameel, Michel De Paepe, Comparison of metal foam heat exchangers to a finned heat exchanger for low reynolds number applications, Int. J. Heat Mass Transfer 89 (2015) 1–9.
[3] Nicola Bianco, Nicola Cherella, Andrea Fragnito, Marcello Iasiello, Gerardo Maria Mauro, Multi-material topology optimization of innovative microchannel heat sinks equipped with metal foams, Int. J. Heat Mass Transfer 222 (2024) 125201.
[4] Prabha Samudre, Satish Vasu Kailas, Thermal performance enhancement in open-pore metal foam and foam-fin heat sinks for electronics cooling, Appl. Therm. Eng. 205 (2022) 117885.
[5] Anurag Kulshreshtha, SK Dhakad, Preparation of metal foam by different methods: A review, Mater. Today: Proc. 26 (2020) 1784–1790.
[6] Ahmed Hassan, Ibrahim Abdullah Alnaser. A review of different manufacturing methods of metallic foams, ACS Omega 9 (6) (2024) 6280–6295.
[7] Matteo Fasano, Luigi Ventola, Flaviana Calignano, Diego Manfredi, Elisa P Ambrosio, Eliodoro Chiavazzo, Pietro Asinari, Passive heat transfer enhancement by 3d printed pitot tube based heat sink, Int. Commun. Heat Mass Transfer 74 (2016) 36–39.
[8] Patricia Fernández-Morales, Emigdio Mendoza Fandiño Lauramaría Echeverrí, Alejandro Alberto Zuleta Gil, Replication casting and additive manufacturing for fabrication of cellular aluminum with periodic topology: optimization by cfd simulation, Int. J. Adv. Manuf. Technol. 126 (3) (2023) 1789–1797.
[9] Mingrui Sun, Guanghan Yan, Chengzhi Hu, Jiafei Zhao, Fei Duan, Yongchen Song, Thermal and hydraulic behaviours of kelvin cells from metallic three-dimensional printing, Appl. Therm. Eng. 219 (2023) 119433.
[10] Mingrui Sun, Lei Yang, Chengzhi Hu, Jiafei Zhao, Dawei Tang, Yongchen Song, Simulation of forced convective heat transfer in kelvin cells with optimized skeletons, Int. J. Heat Mass Transfer 165 (2021) 120637.
[11] Michele Calati, Edoardo De Monte, Simone Mancin, Numerical analysis of the effects of the structure shape and orientation of kelvin cell porous structures during air forced convection, Appl. Sci. 11 (13) (2021) 6189.
[12] Francesco Lucci, Augusto Della Torre, Gianluca Montenegro, Rolf Kaufmann, Panayotis Dimopoulos Eggenschwiler, Comparison of geometrical, momentum and mass transfer characteristics of real foams to kelvin cell lattices for catalyst applications, Int. J. Heat Mass Transfer 108 (2017) 341–350.
[13] Mingrui Sun, Guanghan Yan, Mianbo Ning, Chengzhi Hu, Jiafei Zhao, Fei Duan, Dawei Tang, Yongchen Song, Forced convection heat transfer: a comparison between open-cell metal foams and additive manufactured kelvin cells, Int. Commun. Heat Mass Transfer 138 (2022) 106407.
[14] Mahmoud Abdelmagied, Thermo-fluid characteristics and exergy analysis of a twisted tube helical coil, Sci. Rep. 14 (1) (2024) 27873.
[15] AM Alklaibi, Mahmoud Abdelmagied, A comparative theoretical study of fluid flow and heat transfer in counter flow helical and conical coiled annulus heat exchangers, Comput. Therm. Sci.: An Int. J. (2025).
[16] Mahmoud Abdelmagied, Determining of the thermo-hydraulic characteristics and exergy analysis of a triple helical tube with inner twisted tube, Chem. Eng. Process. - Process. Intensif. 204 (2024) 109922.
[17] Mahmoud M. Abdelmagied, Improving the thermofluid performance of a shell and corrugated coil heat exchanger with novel configurations, J. Therm. Sci. Eng. Appl. 18 (9) (2026) 091004.
[18] Nima Fathi, Mahyar Pourghasemi, Seyed Sobhan Aleyasin, Laura Savoldi, Sal Rodriguez, On conjugate heat transfer in microchannel heat sinks, Int. J. Thermofluids 22 (2024) 100658.
[19] Hossein Ebadi, Diego-César Alarcón-Padilla, Rafael Guedez, Hoda Mahmoudi, Silvia Trevisan, Loreto Valenzuela, Laura Savoldi, Thermal design optimization of a parabolic trough collector receiver with a tube-bundle cavity, Sol. Energy 309 (2026) 114439.
[20] Simone Mancin, Claudio Zilio, Andrea Diani, Luisa Rossetto, Air forced convection through metal foams: Experimental results and modeling, Int. J. Heat Mass Transfer 62 (2013) 112–123.
[21] S Rambabu, P Parthasarathy, et al., A numerical study of forced convection in ideal and randomized reticulated porous structures and a proposal for a new correlation, Int. J. Heat Mass Transfer 184 (2022) 122292.
[22] S Rambabu, K Kartik Sriram, Siddharth Chamarthy, P Parthasarathy, et al., A proposal for a correlation to calculate pressure drop in reticulated porous media with the help of numerical investigation of pressure drop in ideal & randomized reticulated structures, Chem. Eng. Sci. 237 (2021) 116518.
[23] Benjamin Dietrich, Pressure drop correlation for ceramic and metal sponges, Chem. Eng. Sci. 74 (2012) 192–199.
[24] Marcello Iasiello, Salvatore Cunsolo, Nicola Bianco, Wilson KS Chiu, Vincenzo Naso, Developing thermal flow in open-cell foams, Int. J. Therm. Sci. 111 (2017) 129–137.
[25] Inderjot Kaur, Prashant Singh, Flow and thermal transport through unit cell topologies of cubic and octahedron families, Int. J. Heat Mass Transfer 158 (2020) 119784.
[26] Augusto Della Torre, Gianluca Montenegro, Angelo Onorati, G Tabor, Cfd characterization of pressure drop and heat transfer inside porous substrates, Energy Procedia 81 (2015) 836–845.
[27] Andrea Diani, Karthik K Bodla, Luisa Rossetto, Suresh V Garimella, Numerical investigation of pressure drop and heat transfer through reconstructed metal foams and comparison against experiments, Int. J. Heat Mass Transfer 88 (2015) 508–515.
[28] Giuseppe Ambrosio, Nicola Bianco, Wilson KS Chiu, Marcello Iasiello, Vincenzo Naso, Maria Oliviero, The effect of open-cell metal foams strut shape on convection heat transfer and pressure drop, Appl. Therm. Eng. 103 (2016) 333–343.
[29] Olga Soloveva, Sergei Solovev, Ruzil Yafizov, Hydrodynamics and convective heat transfer in open cell foam with micropores, Transp. Res. Procedia 54 (2021) 64–68.
[30] Parham Poureslami, Majid Siavashi, Hamid Moghimi, Milad Hosseini, Pore-scale convection-conduction heat transfer and fluid flow in open-cell metal foams: A three-dimensional multiple-relaxation time lattice boltzmann (mrt-lbm) solution, Int. Commun. Heat Mass Transfer 126 (2021) 105465.
[31] Simone Pusterla, Maurizio Barbato, Alberto Ortona, Claudio D'Angelo, Numerical study of cell morphology effects on convective heat transfer in reticulated ceramics, Int. J. Heat Mass Transfer 55 (25–26) (2012) 7902–7910.
[32] Sebastian Meinicke, Konrad Dubil, Thomas Wetzel, Benjamin Dietrich, Characterization of heat transfer in consolidated, highly porous media using a hybrid-scale cfd approach, Int. J. Heat Mass Transfer 149 (2020) 119201.
[33] Abhay Girija Krishnanunni, Jayakumar Janardhanan Sarasamma, Yepuri Giridhara Babu, Felix Jesuraj, CFD simulation of open-cell aluminum metal foams for pressure drop characterization, in: Gas Turbine India Conference, vol. 35161, American Society of Mechanical Engineers, 2013, V001T04A003.
[34] Mingrui Sun, Lunxiang Zhang, Chengzhi Hu, Jiafei Zhao, Dawei Tang, Yongchen Song, Forced convective heat transfer in optimized kelvin cells to enhance overall performance, Energy 242 (2022) 122995.
[35] Tisha Dixit, Perumal Nithiarasu, Shan Kumar, Numerical evaluation of additively manufactured lattice architectures for heat sink applications, Int. J. Therm. Sci. 159 (2021) 106607.

[36] Karen N Son, Justin A Weibel, Vellaisamy Kumaresan, Suresh V Garimella, Design of multifunctional lattice-frame materials for compact heat exchangers, Int. J. Heat Mass Transfer 115 (2017) 619–629.
[37] Marcello Iasiello, Nicola Bianco, Wilson KS Chiu, Vincenzo Naso, The effects of variable porosity and cell size on the thermal performance of functionally-graded foams, Int. J. Therm. Sci. 160 (2021) 106696.
[38] Ehsan Rezaei, Maurizio Barbato, Sandro Gianella, Alberto Ortona, Sophia Haussener, Pressure drop and convective heat transfer in different sisic structures fabricated by indirect additive manufacturing, J. Heat Transf. 142 (3) (2020) 032702.
[39] Silvia Truscello, Greet Kerckhofs, Simon Van Bael, Grzegorz Pyka, Jan Schrooten, Hans Van Oosterwyck, Prediction of permeability of regular scaffolds for skeletal tissue engineering: a combined computational and experimental study, Acta Biomater. 8 (4) (2012) 1648–1658.
[40] Luigi Ventola, Matteo Fasano, Roberta Cappabianca, Luca Bergamasco, Francesca Clerici, Luciano Scaltrito, Eliodoro Chiavazzo, Pietro Asinari, Convective heat transfer enhancement through laser-etched heat sinks: Elliptic scale-roughened and cones patterns, Energies 13 (6) (2020) 1360.
[41] Marcello Iasiello, Salvatore Cunsolo, Maria Oliviero, William M Harris, Nicola Bianco, Wilson KS Chiu, Vincenzo Naso, Numerical analysis of heat transfer and pressure drop in metal foams for different morphological models, J. Heat Transf. 136 (11) (2014) 112601.
[42] Andrea Diani, Kartik K Bodla, Luisa Rossetto, Suresh V Garimella, Numerical analysis of air flow through metal foams, Energy Procedia 45 (2014) 645–652.
[43] Abhilas Swain, Prashant Kumar Jha, Radha Kanta Sarangi, Satya Prakash Kar, Metal foams for enhanced boiling heat transfer: A comprehensive review, J. Therm. Anal. Calorim. 149 (24) (2024) 14559–14586.
[44] Kaiwen Bai, Zixuan Zhai, Yantao Wu, Changchang Zhang, Hanwen Zhang, Integrated CFD, machine learning and genetic algorithm optimization of metal foam manifold cold plates for energy storage battery thermal management, Energy Rep. 14 (2025) 5488–5504.
[45] Abbas J. Jubear Al-jassani, Ahmed A.Y. Al-Waaly, M. Uglah Aqeel, Goutam Saha, Experimental and numerical evaluations of geometry and structure effects on passive cooling efficiency in metal foam finned heat sinks, Int. J. Heat Fluid Flow 119 (2026) 110300.
[46] Huizhu Yang, Yongyao Li, Binjian Ma, Yonggang Zhu, Review and a theoretical approach on pressure drop correlations of flow through open-cell metal foam, Materials 14 (12) (2021).
[47] Mattia Casini, Paolo De Angelis, Eliodoro Chiavazzo, Luca Bergamasco, Current trends on the use of deep learning methods for image analysis in energy applications, Energy AI 15 (2024) 100330.
[48] Mattia Casini, Paolo De Angelis, Marco Porrati, Paolo Vigo, Matteo Fasano, Eliodoro Chiavazzo, Luca Bergamasco, Machine learning and image analysis towards improved energy management in industry 4.0: a practical case study on quality control, Energy Effic. 17 (5) (2024) 48.
[49] Jiangjiao Li, Jin Han, Dapeng Niu, Xi Zhuo Jiang, Fast and accurate gas turbine emission prediction based on a light and enhanced transformer model, Fuel 376 (2024) 132750.
[50] Laura Savoldi, Andrea Allio, Alberto Leggieri, Optimization of the flow distribution in a gyrotron cavity using evolutionary cfd simulations driven by a genetic algorithm, Int. J. Heat Fluid Flow 96 (2022) 108987.
[51] Giovanni Trezza, Luca Bergamasco, Matteo Fasano, Eliodoro Chiavazzo, Minimal crystallographic descriptors of sorption properties in hypothetical mofs and role in sequential learning optimization, Npj Comput. Mater. 8 (1) (2022) 123.
[52] Shannon A Bonke, Giovanni Trezza, Luca Bergamasco, Hongwei Song, Eliodoro Chiavazzo Santiago Rodríguez-Jiménez, Erwin Reisner, Multi-variable multi-metric optimization of self-assembled photocatalytic co2 reduction performance using machine learning algorithms, J. Am. Chem. Soc. 146 (22) (2024) 15648–15658.
[53] Ansys SpaceClaim, 3D modeling software, 2024, https://www.ansys.com/it-it/products/3d-design/ansys-spaceclaim. (Accessed 04 2024).
[54] Frank P Incropera, David P DeWitt, Theodore L Bergman, Adrienne S Lavine, et al., Fundamentals of Heat and Mass Transfer, vol. 6, Wiley, New York, 1996.
[55] Ansys Fluent, Fluid simulation software, 2024, https://www.ansys.com/products/fluids/ansys-fluent. (Accessed 04 2024).
[56] Joel H Ferziger, Milovan Perić, Robert L Street, Computational methods for fluid dynamics, springer, 2019.
[57] Ismail Tosun, in: Ismail Tosun (Ed.), 4 - Evaluation of Transfer Coefficients: Engineering Correlations, second ed., in: Modeling in Transport Phenomena(Second Edition), Elsevier Science B. V., Amsterdam, 2007, pp. 59–115.
[58] Benjamin Dietrich, Wilhelm Schabel, Matthias Kind, Holger Martin, Pressure drop measurements of ceramic sponges - determining the hydraulic diameter, Chem. Eng. Sci. 64 (16) (2009) 3633–3640.
[59] Riccardo Poli, John Koza. Genetic programming, Search Methodologies: Introductory Tutorials in Optimization and Decision Support Techniques, Springer, 2013, pp. 143–185.
[60] Dimitrios Angelis, Filippos Sofos, Theodoros E Karakasidis, Artificial intelligence in physical sciences: Symbolic regression trends and perspectives, Arch. Comput. Methods Eng. 30 (6) (2023) 3845–3865.
[61] HeuristicLabWiki, Symbolic regression problem, 2011.
[62] Riccardo Poli, B. Langdon William, Nicholas F. McPhee, A Field Guide To Genetic Programming, Lulu Press, Raleigh, NC, USA, 2008.
[63] Claudio Ferroni, Federico Sascha Franchi, Matteo Ambrosetti, Mauro Bracconi, Gianpiero Groppi, Matteo Maestri, Enrico Tronconi, Numerical and experimental investigation of pressure drop in periodic open cellular structures for intensification of catalytic processes, ACS Eng. Au 2 (2) (2022) 118–133.
[64] Jacob Bear, Dynamics of Fluids in Porous Media, Elsevier, New York, USA, 1972.
[65] Jin Yao Ho, Kai Choong Leong, Teck Neng Wong, Experimental and numerical investigation of forced convection heat transfer in porous lattice structures produced by selective laser melting, Int. J. Therm. Sci. 137 (2019) 276–287.
[66] Mingrui Sun, Yiqiang Liang, Xizhuo Jiang, Yongchen Song, Flow and heat transfer characteristics of anisotropic kelvin cells: Influence of stretching ratio and mechanistic analysis, Int. Commun. Heat Mass Transfer 169 (2025) 109896.
[67] Pauli Virtanen, Ralf Gommers, Travis E Oliphant, Matt Haberland, Tyler Reddy, David Cournapeau, Evgeni Burovski, Pearu Peterson, Warren Weckesser, Jonathan Bright, et al., Scipy 1.0: fundamental algorithms for scientific computing in python, Nature Methods 17 (3) (2020) 261–272.
[68] A Kopanidis, A Theodorakakos, E Gavaises, D Bouris, 3D numerical simulation of flow and conjugate heat transfer through a pore scale model of high porosity open cell metal foam, Int. J. Heat Mass Transfer 53 (11–12) (2010) 2539–2550.
[69] Varaprasad V. Calmidi, Transport Phenomena in High Porosity Fibrous Metal Foams, (Ph.D. thesis), University of Colorado at Boulder, Boulder, CO, USA, 1998.
[70] Nihad Dukhan, Pragnesh Patel, Equivalent particle diameter and length scale for pressure drop in porous metals, Exp. Therm. Fluid Sci. 32 (5) (2008) 1059–1067.